Origin of iodine preferential attack at sulfur in phosphorothioate and subsequent P-O or P-S bond dissociation

Qiang Huang[a,b,1], Ga Young Lee[c,1], Jiayi Li[a,b,1], Chuan Wang[a,b], Rosalinda L. Zhao[c], Zixin Deng[a,b], K. N. Houk[c,2], and Yi-Lei Zhao[a,b,2]

Iodine-induced cleavage at phosphorothioate DNA (PT-DNA) is characterized by extremely high sensitivity (∼1 phosphorothioate link per 10^6 nucleotides), which has been used for detecting and sequencing PT-DNA in bacteria. Despite its foreseeable potential for wide applications, the cleavage mechanism at the PT-modified site has not been well established, and it remains unknown as to whether or not cleavage of the bridging P-O occurs at every PT-modified site. In this work, we conducted accurate ωB97X-D calculations and high-performance liquid chromatography-mass spectrometry to investigate the process of PT-DNA cleavage at the atomic and molecular levels. We have found that iodine chemoselectively binds to the sulfur atom of the phosphorothioate link via a strong halogen-chalcogen interaction (a type of halogen bond, with binding affinity as high as 14.9 kcal/mol) and thus triggers P-O bond cleavage via phosphotriester-like hydrolysis. Additionally, aside from cleavage of the bridging P-O bond, the downstream hydrolyses lead to unwanted P-S/P-O conversions and a loss of the phosphorothioate handle. The mechanism we outline helps to explain specific selectivity at the PT-modified site but also predicts the dynamic stoichiometry of P-S and P-O bond breaking. For instance, Tris is involved in the cascade derivation of *S*-iodo-phosphorothioate to *S*-amino-phosphorothioate, suppressing the *S*-iodo-phosphorothioate hydrolysis to a phosphate diester. However, hydrolysis of one-third of the Tris-O-grafting phosphotriester results in unwanted P-S/P-O conversions. Our study suggests that bacterial DNA phosphorothioation may more frequently occur than previous bioinformatic estimations have predicted from iodine-induced deep sequencing data.

DNA phosphorothioation | DNA cleavage | halogen bond | mass spectroscopy analysis | computational analysis

Bacterial DNA phosphorothioation is the replacement of a nonbridging oxygen atom with a sulfur atom in the phosphodiester linkage of the DNA backbone by functional gene clusters such as type I *dnd*ABCDE in *Streptomyces lividans* (1) and type II *ssp*ABCD in *Vibrio cyclitrophicus* FF75 (2). The physiologically phosphorothioate DNA (PT-DNA) constitutes a modification-restriction system with a partner gene cluster like *ssp*E or *dnd*FGH to distinguish non–PT-modified foreign DNA (2, 3). The DNA phosphorothioation is physically recognized by the molecular interaction of the sulfur binding domain (SBD) in the *Streptomyces coelicolor* type IV restriction enzyme ScoMcrA (4, 5). Moreover, phosphorothioate chemistry confers PT-DNA antioxidant activity to repair oxidative damage caused by hydrogen peroxide and peracetic acid (6, 7) and even peroxynitrious acid (8), in which PT-DNA is converted back to normal DNA and forms sulfur oxide products. As shown in Fig. 1, compared with the complicated gene-editing molecular machine ScoMcrA (4, 5), iodine (I_2) is able to selectively cleave the P-O bridging bond at the PT-DNA phosphorothioate site and can thereby potentially be used to detect, quantify, and map PT-containing bacterial genomes (9–11).

The reaction mechanism for the iodine-induced PT-DNA cleavage (Fig. 1, path 4) is illusive, in part because the P-S/P-O reversion usually dominates, and the P-O scission rarely occurs during most antioxidant reactions (Fig. 1, path 2) (6–8). For instance, in the presence of hydrogen peroxide and peroxynitrite, the P-S/P-O reversion converts the phosphorothioate diester to a normal phosphate DNA linkage (loss of the PT handle) and provides multiple electrons to quench additional reactive oxygen species (ROS). In the presence of hypochlorous acid, liquid chromatography-mass spectrometry (LC-MS) analysis was used to show that a considerable amount of P-S/P-O transformation was observed, along with instability in the PT genome (12, 13). Even though molecular iodine is able to act as an oxidant (as in Fig. 1, path 2), previous studies of iodine-induced PT-DNA cleavage did not address the potential competition between the P-S/P-O reversion and P-O scission; the bioinformatics analysis of these studies assumed an equivalent (if not fully) P-O cleavage occurring at all the

Significance

Iodine-induced cleavage is widely used for detecting bacterial DNA phosphorothioation in gel electrophoresis, deep sequencing, and single-molecule optical mapping. However, we lack quantitative understanding of the phosphorothioate DNA (PT-DNA) cleavage efficiency and the chemoselectivity of this method for determination of phosphorothioate vs. phosphate. Computational explorations now reveal why iodine selectively attacks at sulfur in phosphorothioate links but not at normal phosphates. The active role of Tris buffer in the PT-DNA cleavage, and the factors controlling cleavage efficiency, were also revealed. Cleavage efficiency is limited by competition between the desired DNA backbone cleavage and unwanted P-S/P-O conversion. These mechanistic studies will guide the development of new methods for iodine-induced specific PT-DNA cleavage.

[1]Q.H., G.Y.L., and J.L. contributed equally to this work.

[2]To whom correspondence may be addressed. Email: houk@chem.ucla.edu or yileizhao@sjtu.edu.cn.
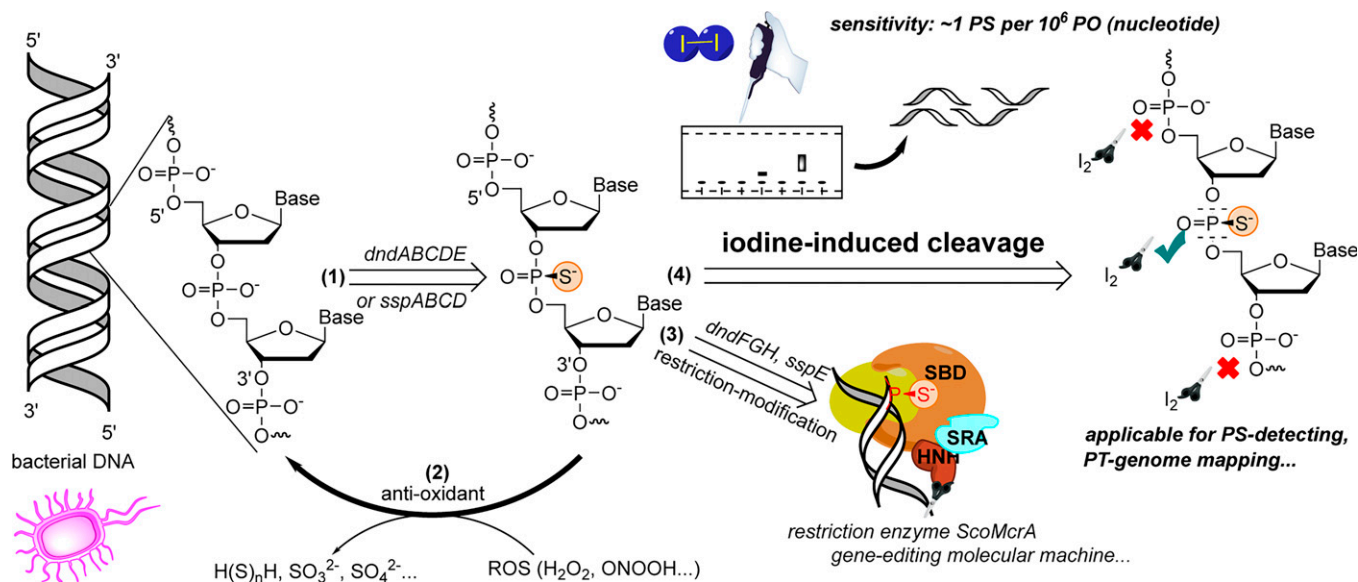
Fig. 1. PT-DNA generation and its specific roles in biology and chemistry. Path 1 shows that gene clusters *dnd*ABCDE and *ssp*ABCD transform a phosphate subunit in a particular sequence pattern to a phosphorothioate linkage. Path 2 shows the antioxidant chemistry of PT-DNA, which protects bacterial genomes from oxidative damage of ROS species. Path 3 shows that gene clusters *dnd*FGH and *ssp*E constitute specific restriction-modification systems. ScoMcrA is a type IV modification-dependent restriction endonuclease that consists of a SBD distinguishing the target PT-DNA and a phosphate diester hydrolase (HNH). SRA is a methyl-DNA binding "SET and RING-associated" domain. Path 4 shows that iodine-induced cleavage directly breaks down the P-O bridging bonds at the PT-modified site.

PT-modified sites (9–11). In order to accurately map the PT genome, it is crucial to know the probability of the dissociation of the bridging P-O bond in the iodine-induced PT site–specific scission; consequently, it is necessary to distinguish the detailed reaction mechanisms between iodine and phosphorothiate or iodine and phosphate.

Even though the iodine-induced phosphorothionucleotide cleavage was first proposed more than three decades ago by Eckstein and coworkers (14, 15), recent studies have failed to explain the actual role of iodine in this process. It has been suggested that iodine-induced cleavage stemmed from 2-iodoethanol–conjugated phosphorothioate alkylation (11), but the simple mixture of iodine and ethanol under ambient conditions cannot generate 2-iodoethanol, the so-called active alkylating reagent in iodine-induced cleavage reactions. Therefore, a more comprehensive understanding is required for the purpose of developing the iodine-PT deep sequencing protocol for biotechnology; otherwise, bioinformatic analysis based on the assumption of breaking all-phosphorothioate linkages would give misleading PT-modified information about bacterial PT genomes.

Moreover, the rapid rupture of the bridging P-O bonds in phosphorothioate diesters apparently violates phosphoryl-transfer biochemistry (16, 17). In the absence of phosphodiesterase, the bridging P-O bond in DNA is exceptionally stable, with a theoretical half-life of 30 million y at 25 °C (18). The thio effect of phosphorothioate substitution further enhances the antihydrolytic stability of this linkage by one or two orders of magnitude, and this substitution is widely used in developing stable antisense RNA drugs (19, 20). Thus, revealing the unique "click" chemistry of iodine-induced PT-DNA cleavage at the hydrolysis-resistant PT site has significant implications for both biotechnology and drug discovery.

We have performed density functional theory (DFT) calculations to 1) interrogate the extremely high chemoselectivity between iodine-phosphorothioate and iodine-phosphate and 2) determine the enhanced rate of bridging P-O bond scissions in the iodine-phosphorothioate derivatives. We have discovered that

iodine and phosphorothioate selectively form a significantly strong halogen-chalcogen bond. After release of an iodide ion, the resulting iodine-phosphorothioate complex [**PS⁻●I₂**] is able to convert the hydrolysis-resistant phosphorothioate diester to a hydrolysis-vulnerable phosphotriester-like structure. The hydrolytic dissociation of the bridging P-O bonds at the PT site is significantly promoted in the downstream phosphotriester species, such as the Tris-O-grafting phosphotriester and other S-amino-phosphorothioates (**PSN**s), affording nucleophilic substitution by amine groups from Tris buffer and DNA bases. The Tris-O-grafting phosphorotriester dominates these conversions via internal cyclization of its hydroxyl branches. Our findings successfully illustrate the comprehensive mechanistic cascade processes of iodine adduction, iodide elimination, nucleophilic substitution, and P-O/P-S bond dissociation in iodine-induced PT-DNA cleavage.

Results

The Halogen-Chalcogen Interaction of Phosphorothioate and iodine. In order to elucidate the mechanism of iodine's preferential attack at the phosphorothioate site, we began by investigating possible molecular interactions between the DNA backbones and iodine. We calculated Gibbs free energies for the 3-center-4-electron (3c-4e) halogen bonding (XB) interaction of iodine with phosphorothioate, phosphate, and iodide in aqueous solution. The complexes formed by phosphorothioate diester (**PS**, **4**) or phosphate diester (**PO**, **1**) with I₂ were compared at the ωB97X-D/cc-pVTZ/LanL2DZ(I)/SMD(water) level of theory (SMD, solvation model based on density). The free energy of complex formation for phosphorothioate and iodine (**5**) was calculated to be −14.9 kcal/mol, while that of phosphate and iodine (**2**) is unfavorable by +1.3 kcal/mol at room temperature (Fig. 2A). The large negative free energy of the halogen-chalcogen interaction is much more significant than that of the [I⁻●I₂] interaction, which is the strongest halogen bond reported in the literature to date (I⁻ + I₂ = I₃⁻, $\Delta H_{cal.} = -8.5$ kcal/mol and $\Delta G_{cal.} = +0.8$ kcal/mol) (21, 22).
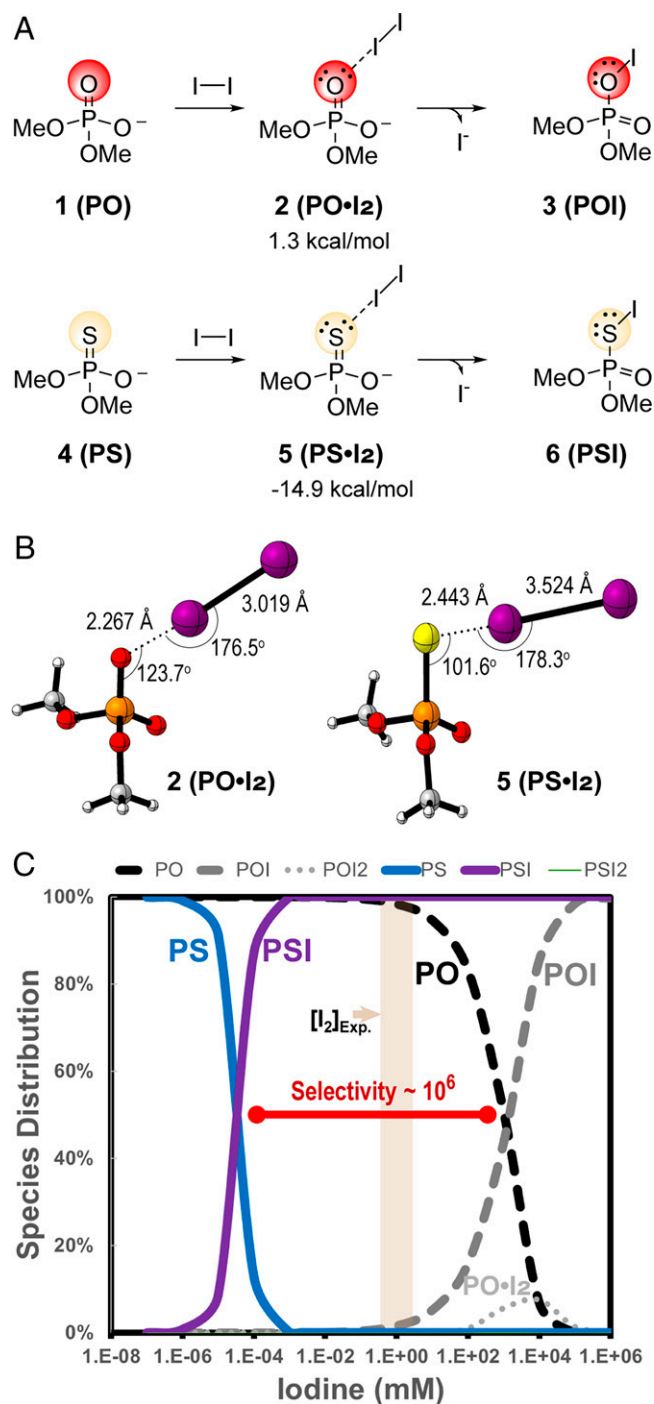
Fig. 2. XB formation and the resulting cleavage selectivity of (*A*) the halogen-chalcogen type of XB formation between iodine and phosphate backbone (*Top*) and the halogen-chalcogen type of XB formation between iodine and thiophosphate backbone (*Bottom*). Free energies (ΔG_{aq}) were calculated at the ωB97X-D/cc-pVTZ/LanL2DZ (I)/SMD(water) level of theory. (*B*) Computed geometries of XB complexes, **2** and **5**. (*C*) The theoretical partitions of **PS**-**PSI** and **PO**-**POI** conversion at variant concentrations of iodine, where $[PS]_0 = 0.115$ μM and $[PO]_0 = 76.5$ μM in an $OD_{260} = 0.5$ PT-DNA solution.

We calculated the highest-energy occupied molecular orbital (HOMO) and the lowest-energy unoccupied molecular orbital (LUMO) gaps to examine the origin of the unprecedented I_2-chalcogen interaction, which has an enthalpy change of −22.4 kcal/mol. For comparison, the $I_2 — I^-$ interaction is computed to be −8.5 kcal/mol for the strong halogen bond in I_3^-. In the 3c-4e sigma bond system, the higher-energy HOMO (−2.46 eV) of phosphorothioate may donate electrons to the LUMO (anti-σ*, −4.95 eV) of iodine more efficiently than the lower-energy HOMO (−3.31 eV) of phosphate; moreover, the high-energy sulfur 3p lone pair electrons may also be involved in π-bond interactions (*SI Appendix,* Fig. S1). These interactions were visualized by the typical representation of reduced density gradient of ring and cloud regions in the spatial electron density gradient analysis for noncovalent interactions (*SI Appendix,* Fig. S2).

The halogen-chalcogen complexes of phosphorothioate and iodine can decompose into *S*-iodo-phosphorothioate (**PSI**, **6**) via release of an iodide anion. Although this process is computed to be endothermic by 3.0 kcal/mol in enthalpy, it benefited from an entropic gain; its Gibbs free energy is calculated to be exergonic at room temperature by −3.1 kcal/mol. For comparison, the hypothetical decomposition of **PO•I₂** (**2**) to **POI** (**3**) was computed to be unfavorable in both enthalpy (+10.9 kcal/mol) and free energy (+5.0 kcal/mol). Thus, the strong halogen-chalcogen interaction between phosphorothioate (**PS**, **4**) and I_2 decreases the covalent I-I bond significantly, leading to heterogeneous dissociation of the I-I bond (the I-I bond length elongates by 0.5 Å in the XB complex) (Fig. 2*B*). We also employed COPASI (the Complex Pathway Simulator package; see the details in the computational section of *Materials and Methods*) to simulate the halogen-chalcogen complex formation and consequent I-I dissociation using the high-level quantum-mechanics (QM)-calculated Gibbs free energies. The initial concentrations of **PO** (**1**) and **PS** (**4**) were estimated using the iodine/PT-plasmid experiment, where [**PS**] = ~0.115 μM and [**PO**] = ~76.5 μM for OD_{260} (absorbance at 260 nm) = 0.5 plasmid solution (equivalently ~25 μg/mL double-stranded DNA, assuming that 0.15% of PO linkages were physiologically modified to PS by the *dnd* gene) (Fig. 1, path 1). The phosphospecies response distinguished between different iodine concentrations in the hypothetical equilibria toward **POI** (**3**) and **PSI** (**6**). As shown in Fig. 2*C*, the COPASI simulation indicates that **PS** (**4**) reacts with iodine stoichiometrically, while **PO** (**1**) requires a much higher iodine concentration to form **POI** (**3**). At the half-half transformation (**PX**: **PXI** = 1:1, where **X** = S or O), the hypothetical iodine concentrations were calculated to be 10^{-4} and 10^2 mM, respectively. Thus, the chemoselectivity of iodine at the PT site reaches about ~10^6 under experimental conditions ([I_2] in the millimolar range), by which the phosphorothioate at the PT-modified site is fully converted to the **PSI** (**6**) species, and the inert phosphate linkage in the DNA molecule was unchanged. This result is consistent with the observed cleavage taking place exclusively at the PT site. In the iodine-induced experiment, however, 30 mM iodine was overdosed unless the real PT-modification frequency was over 1,500/10^6 nt.

Nevertheless, the halogen-chalcogen interaction, a distinctive type of halogen bond, conveys a chemoselective attack preferentially at the PT site and converts the hydrolysis-resistant phosphodiester **PS** (**4**) to a hydrolysis-vulnerable phosphotriester-like **PSI** (**6**). Since P-O bond hydrolysis of the phosphate triester is much faster than that of the phosphodiester (23), we next explored possible phosphotriester-like derivatives from the active species **PSI** (**6**), which can transform the nucleophilic sulfur in **PS** (**4**) to an electrophilic sulfur in **PSI** (**6**) that is able to react with available nucleophiles.

Possible Triester-Like Structures Derived from Nucleophilic Substitution at the Sulfur Site. **PSI** is activated and possesses two electrophilic sites: S and P. Before investigating the
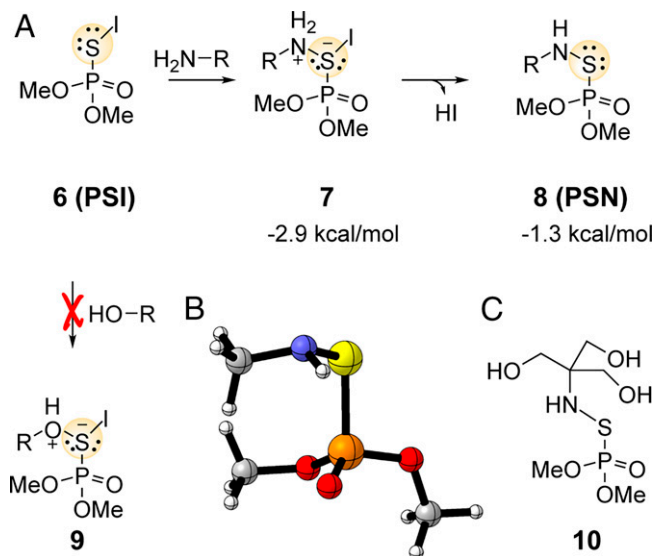
Fig. 3. A_N of amine to the sulfur atom of **PSI**. (A) The reaction ΔG_{aq} of the S-I to S-N transformation (*Top*). S-I to S-O formation does not give a stable intermediate (*Bottom*). (B) Computed geometry of **PSN** (**8**). (C) Tris-*N*-grafting **PSN** (**10**).

electrophilic phosphorus site, we computationally tested the electrophilic sulfur region against a variety of nucleophiles available in the experiments. Two types of nucleophiles were accessible: *N*-containing nucleophiles, such as DNA bases and Tris buffer (amine group), or *O*-containing nucleophiles, such as 3′-hydroxyl ends of DNA, water, and Tris buffer (alcohol branches). Both class of nucleophiles were tested for nucleophilic addition (A_N) to **PSI** using the methylamine and methanol models. As shown in Fig. 3, the S-N coupling was validated to be feasible between **PSI** and amine, while the hydroxyl group was unreactive to **PSI**.

The formation of the S-N bond was nearly barrier free between **PSI** and amine, with an activation energy of 0.94 kcal/mol (diffusion controlled owing to entropy loss of the bimolecular reaction, ~36 J•K^{-1}) (*SI Appendix*, Fig. S3). The A_N was exothermic by −15.0 kcal/mol in enthalpy and −2.9 kcal/mol in Gibbs free energy. The zwitterionic adduct (**7**) spontaneously transforms to **PSN** (**8**) via iodide elimination (−1.3 kcal/mol in free energy) and deprotonation of phosphorosulfenylammonium in aqueous solution (24).

When methanol is used as a nucleophile, no theoretical adduct was observed, though a similar hydrogen bond is formed between the nonbridging oxygen and the hydroxyl group (*SI Appendix*, Fig. S3). One straightforward rationale for this observation is that alcohol is less nucleophilic and the conjugate acid (phosphorosulfenyloxonium) formed by attack of the hydroxyl group is much stronger than the conjugate acid (phosphorosulfenylammonium) formed by the attack of the amine (25).

Secondary amines can also lead to the formation of nucleophilic adducts, but they are higher in activation energy and free energy. Thus, the **PSN** was likely formed via nucleophilic substitution by primary amines like Tris and the sp^3-hybridized nitrogen (-NH$_2$) of the amine-containing DNA bases A, G, and C. It should be noted that Tris possesses primary amine substituents to form Tris-*N*-grafting **PSN** (**10**) (Fig. 3C). In the iodine-cleavage deep sequencing (ICDS), genomic DNA was mixed with iodine and heated up to 65 °C for 5 min to maximize the cleavage (9). The temperature 65 °C is approximately the melting point of DNA primers of a 25-nt length, which may unwind compact DNA molecules to expose the

primary amine substituents of DNA bases in the previous experiments (9). However, genomic/longer DNA won't melt at this temperature, and the heat-up effect might be negligible to expose DNA bases. In addition, the amines of DNA bases are usually solvent exposed in the major and minor grooves, which may modify their base ionization constant values and nucleophilicity due to base-base hydrogen bonds.

Hypothetically, all three types of phosphotriester-like species (**6**, **8**, and **10**) are susceptible to nucleophilic attack at the electrophilic phosphorus, which can lead to competitive P-O and P-S cleavage.

Competitive P-S and P-O Dissociations in the Phosphotriester-Like Species. The P-O and P-S bond dissociations of the above phosphotriesters were calculated at the ωB97X-D/6-31+G(d)/I(LANL2DZ)/SMD(water) level of theory, as previously described (26, 27). Both spontaneous and base-assisted transition structures were extensively searched (28, 29). Since spontaneous phosphoryl transfers have high activation energies, in a range of 31.5 to 43.8 kcal/mol (see the details in *SI Appendix*, Fig. S4), we chose to focus on the base-catalyzed P-O and P-S dissociations of the thiophosphotriester-like species (**6**, **8**, and **10**) due to the availability primary amines in either DNA bases or Tris buffer.

PSI. The spontaneous hydrolysis of **PSI** was calculated to be slow due to the high activation free energy ($\Delta G_{aq}^{\neq}$) of nucleophilic association (41.4 kcal/mol). The resulting pentacoordinate phosphorane intermediate underwent either P-O dissociation (transition state **TS$_D$-PO**, 38.7 kcal/mol) or P-S dissociation (transition state **TS$_D$-PS**, 26.2 kcal/mol) (*SI Appendix*, Fig. S4).

Alternatively, in the presence of a primary amine, **PSI** undergoes a relatively lower-energy and single-step nucleophilic substitution (S_N2). As shown in Fig. 4A, we carried out a model calculation with methylamine to mimic the primary amine group in either DNA bases or Tris buffer. Only the dissociation of the P-S bond was observed in computation, because the SI$^-$ anion is a better leaving group than the alkoxide or hydroxide ions. The calculated $\Delta G_{aq}^{\neq}$ was estimated to be 28.4 kcal/mol at the

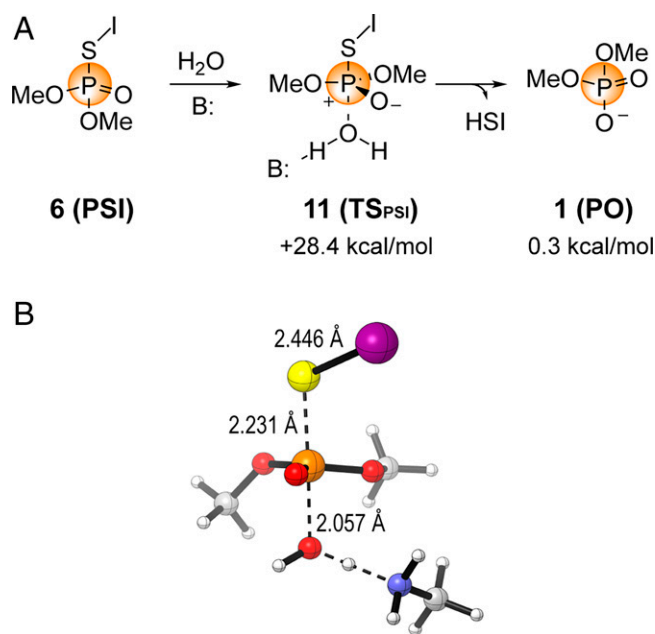**Fig. 4.** S_N2 substitution of PSI. (A) The activation and reaction ΔG_{aq} of the **PSI** to **PO** transformation. The bridging P-O dissociation is not observed in computational base-assisted hydrolysis. (B) Computed geometry of **11**. The activation energy was estimated with reference to a zwitterionic complex because of the barrier-free association of **PSI** + CH$_3$NH$_2$ → PSNH$_2$CH$_3^+$•I$^-$ (**7**).

ωB97X-D/6-31+G(d)/I(LANL2DZ)/SMD(water) level of theory, and the overall hydrolytic reaction was nearly thermoneutral.

It should be noted that the nucleophilic adduction of a primary amine at the sulfur atom is competitive with the base-assisted **PSI** hydrolysis and feasibly leads to the formation of **PSN** (**8**), as in Fig. 3. Here, the primary amine is used as a general base to enhance the nucleophilicity of a water molecule for the hypothetical hydrolysis of **PSI** (**8**). If a primary amine is replaced by a hydroxide (a strong base, [OH⁻] = 0.010 mM at pH 9.0) (30), the activation energy for the hydroxide-assisted **PSI** hydrolysis decreased to 11.4 kcal/mol under standard conditions (temperature = 298.15 K, 1 atm) (*SI Appendix,* Fig. S5).

PSN. The spontaneous hydrolysis of **PSN** is similar to that of the **PSI** species. The $\Delta G_{aq}^{\neq}$ for nucleophilic substitution is calculated to be 43.8 kcal/mol. The phosphorane intermediate can dissociate by either P-O (**TS$_D$-PO**, 36.1 kcal/mol) or P-S (**TS$_D$-PS**, 37.8 kcal/mol) scission (*SI Appendix,* Fig. S4).

Similarly, the association-dissociation process can be significantly accelerated when a primary amine is involved. Using the methylamine base model, these $\Delta G_{aq}^{\neq}$ decrease to 21.6 kcal/mol (**12**, **TS$_A$**, a transition state for association reaction), 11.7 kcal/mol (**14**, **TS$_D$-PO**, a transition state for the bridging P-Ome bond dissociation), and 17.2 kcal/mol (**16**, **TS$_D$-PS**, a transition state for the P-S bond dissociation) (Fig. 5*A*).

In comparison to **PSI** hydrolysis, the P-S bond dissociation of the **PSN** species is much exothermic when releasing sulfenamine, but this process required a higher activation energy (5.5 kcal/mol) than the P-O bond dissociation (Fig. 5*B*). Intriguingly, the bridging P-O bond dissociation was selectively promoted in the **PSN** species; however, the rate-determining step was A$_N$ in the hydrolytic process, indicating the hydrolytic reaction needs a stronger base to promote nucleophilic attack.

Tris-*N*-grafting PSN. The unimolecular cyclization of Tris-*N*-grafting **PSN** (**10**) provides a feasible route for A$_N$. Tris-*N*-grafting denotes a S-N covalent bond with the Tris amine
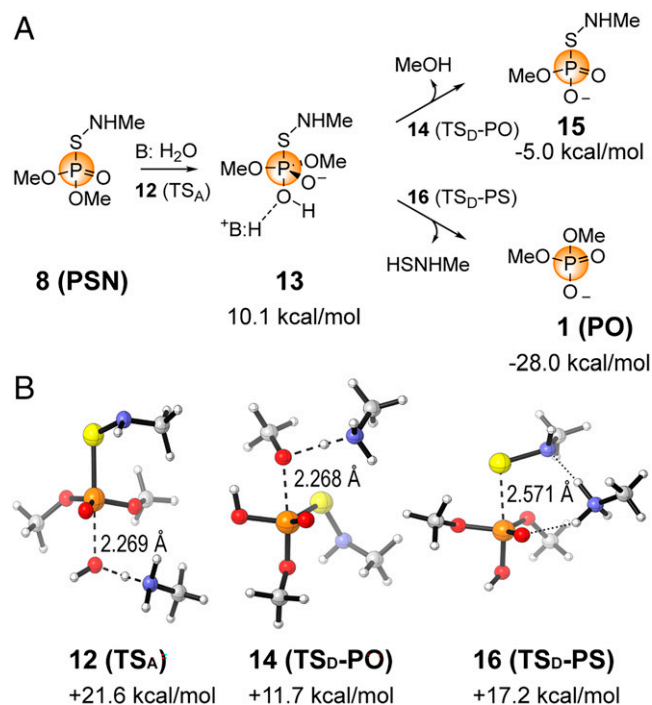
Fig. 5. The associative-dissociative (A$_N$-D$_N$) mechanisms of **PSN** hydrolysis. (*A*) The reaction ΔG_{aq} of **PSN** to **PO** dissociation (*Top*) and **PS** dissociation (*Bottom*). (*B*) Computed geometries of transition states of **12**, **14**, and **16**.
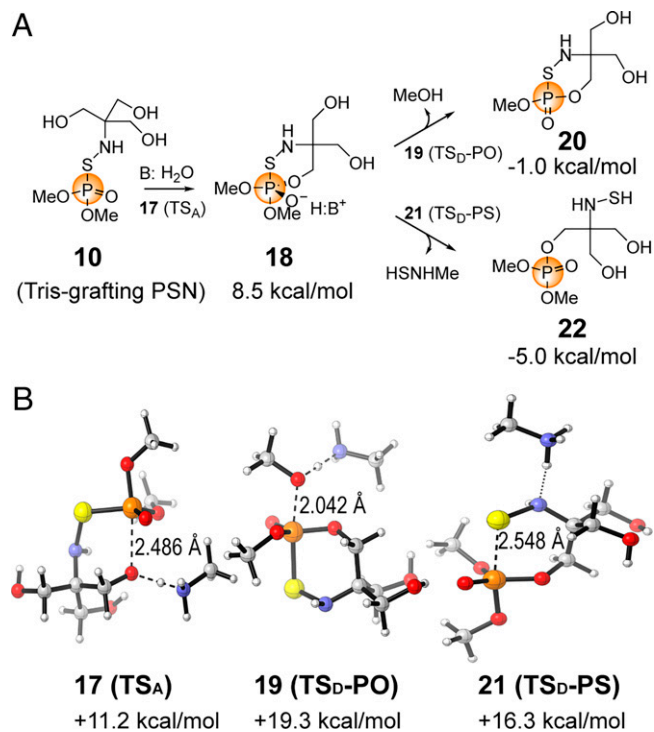
Fig. 6. A$_N$-D$_N$ mechanisms of Tris-*N*-grafting **PSN**. (*A*) The reaction ΔG_{aq} of **PSN** to P-O dissociation (*Top*) and P-S dissociation (*Bottom*). (*B*) Computed geometries of **17**, **19**, and **21**.

group in the **PSN**, allowing intramolecular attacks of Tris hydroxyl groups to the **PSN** electrophilic phosphor center. The activation energy for the spontaneous cyclization was calculated to be 31.5 kcal/mol, which was lower by 12.3 kcal/mol than **PSN** (**8**) for the less entropic loss in the unimolecular reaction. However, the P-O and P-S bond dissociations of the cyclic Tris-N,O-grafting phosphorane intermediate) (**18**) had higher $\Delta G_{aq}^{\neq}$: 34.2 and 34.7 kcal/mol in the absence of base catalysis, respectively (*SI Appendix,* Fig. S4).

With this Tris, instead of a water molecule, the nucleophilic cyclization involves a branching alcohol group for grafting to Tris. The P-S and P-O bond dissociations of the cyclic phosphorane did not break down the Tris-*N*-grafting triester-like species to hydrolysis-inert diesters as in Fig. 5. Instead, this process generated the second generation of hydrolysis-vulnerable triesters.

In the presence of primary amine such as the second Tris molecule or a DNA base, the associative-dissociative (A$_N$-D$_N$) process was also accelerated. Within the methylamine base model, these $\Delta G_{aq}^{\neq}$ decreased to 11.2 kcal/mol (**17**, **TS$_A$**), 19.3 kcal/mol (**19**, **TS$_D$-PO**, bridging P-Ome bond dissociation), and 16.3 kcal/mol (**21**, **TS$_D$-PS**, P-S bond dissociation) (Fig. 6*A*).

We found that the bridging P-O bond dissociation was higher by 3.0 kcal/mol in $\Delta G_{aq}^{\neq}$ than the P-S bond dissociation, which was an unexpected result (Fig. 6*B*). Compared transition state **19** with the geometry of transition state **14** (**TS$_D$-PO**), it is likely that the equatorial hydroxyl group in transition state **14** dramatically stabilized the leaving alkoxide by about 7.6 kcal/mol, probably via a hydrogen-bonding interaction. Consequently, the P-S bond cleavage became a major pathway for the Tris-*N*-grafting **PSN**, which led to a typical phosphotriester (**22**).

We also computed the cascade association-dissociation for the derivative phosphotriester (**22**) based on the assumption of a rapid disproportionation with another primary amine like
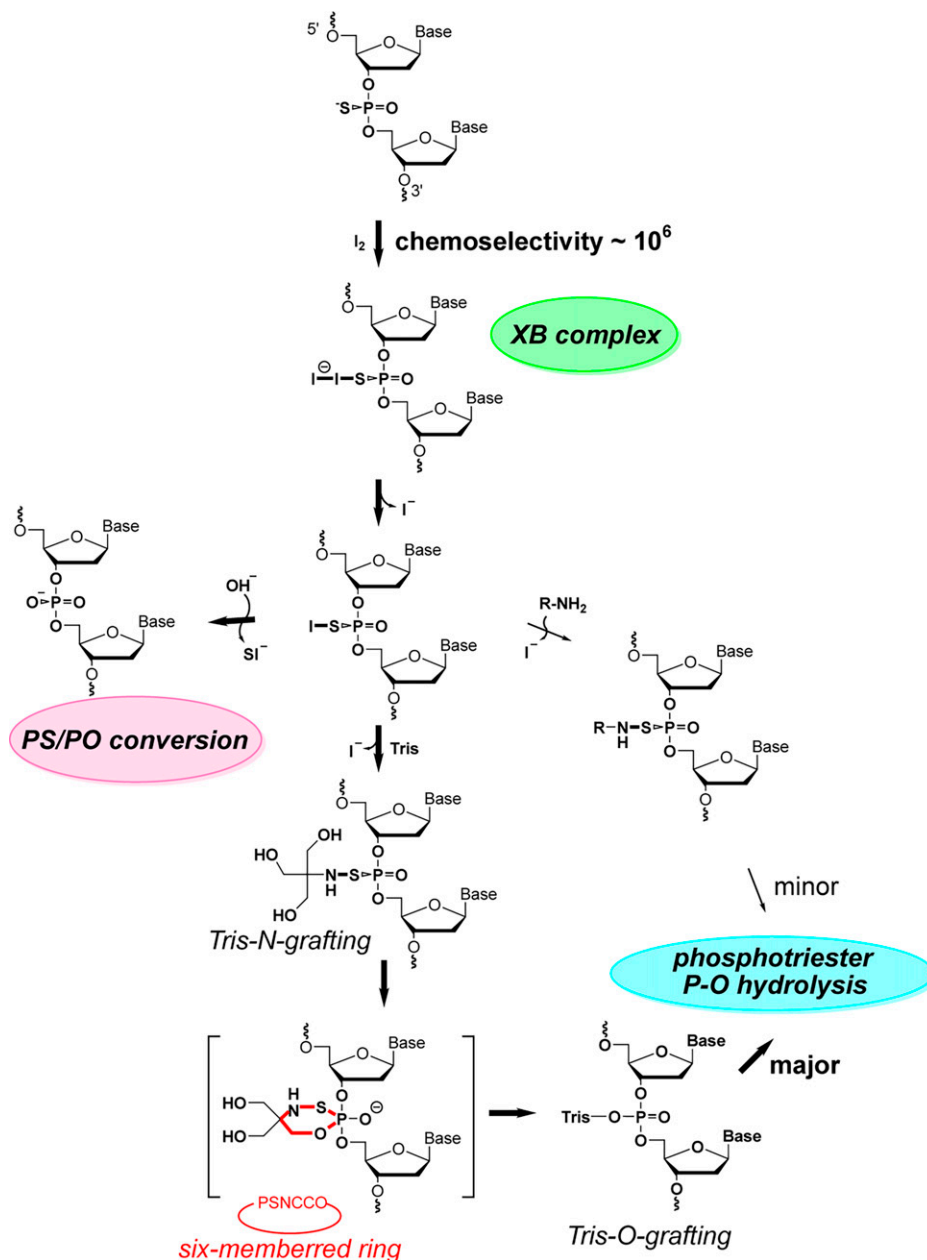
Fig. 7. The competitive P-O and P-S cleavages in the iodine-induced cascade reactions of PT-DNA, where the multiple nucleophilic associations-dissociations lead to both the desired DNA fragmentation and the unwanted P-S/P-O conversion. A high concentration of Tris buffer leads to rapid formation of the relatively stable "PSNCCO" 6-m-r pentaphosphorane intermediate, which dominates the PT-DNA degradation.

Tris buffer ($HSNHR + NH_2R' \rightarrow NH_2R + HSNHR'$, as shown in *SI Appendix*, Fig. S6) (31–33). The $\Delta G_{aq}^{\neq}$ of the base-assisted self-association with the terminal primary amine was calculated to be 21.4 kcal/mol, while that of the consequent P-O bond dissociation was 23.4 kcal/mol (*SI Appendix*, Fig. S7). The cascade association-dissociation for the third generation of phosphotriester was calculated to be 23.8 and 20.6 kcal/mol in $\Delta G_{aq}^{\neq}$, respectively. Therefore, the second-generation phosphotriester (**22**) slowly decomposes to a hydrolysis-inert phosphate diester under conditions typical for DNA experiments (34). Because the three bridging P-O bonds in the phosphotriester (**22**) are chemically equal in terms of cascade hydrolysis, there are two chances to break down the three P-O bridges into two DNA fragments.

In summary, our computational exploration of P-O bond dissociation at the PT-modified site suggests the following: 1) straightforward hydrolysis for the original **PSI** (**6**) recovers the phosphate

linkage and leads to the P-S/P-O conversion; 2) the amine-derivative **PSN** (**8**) selectively cleaves the bridging P-O bond, which was favorable for the cleavage of iodine-induced PT-DNA, but this step has a relatively high activation barrier for the formation of the pentaphosphorane intermediate; and 3) the Tris-*N*-grafting **PSN** (**10**) rapidly transforms to the next generation of Tris-O-grafting phosphotriester (**22**), resulting in a two-thirds chance for the dissociation of the bridging P-O bond. The overall diagram for the iodine-induced PT-DNA cleavage is shown in Fig. 7.

Experimental Validation. We validated the speculative Tris effects with modified conditions for iodine-induced treatments, in which phosphate buffer was purposely replaced with Tris. The plasmid agarose gel electrophoresis of PT-containing plasmid was consistent with our earlier studies (*SI Appendix*, Figs. S8–S10, figure S2 in 7, and figure S3 in ref. 8). Two PT dinucleotides ($G_{PS}G$ and $G_{PS}A$, the most abundant PT-
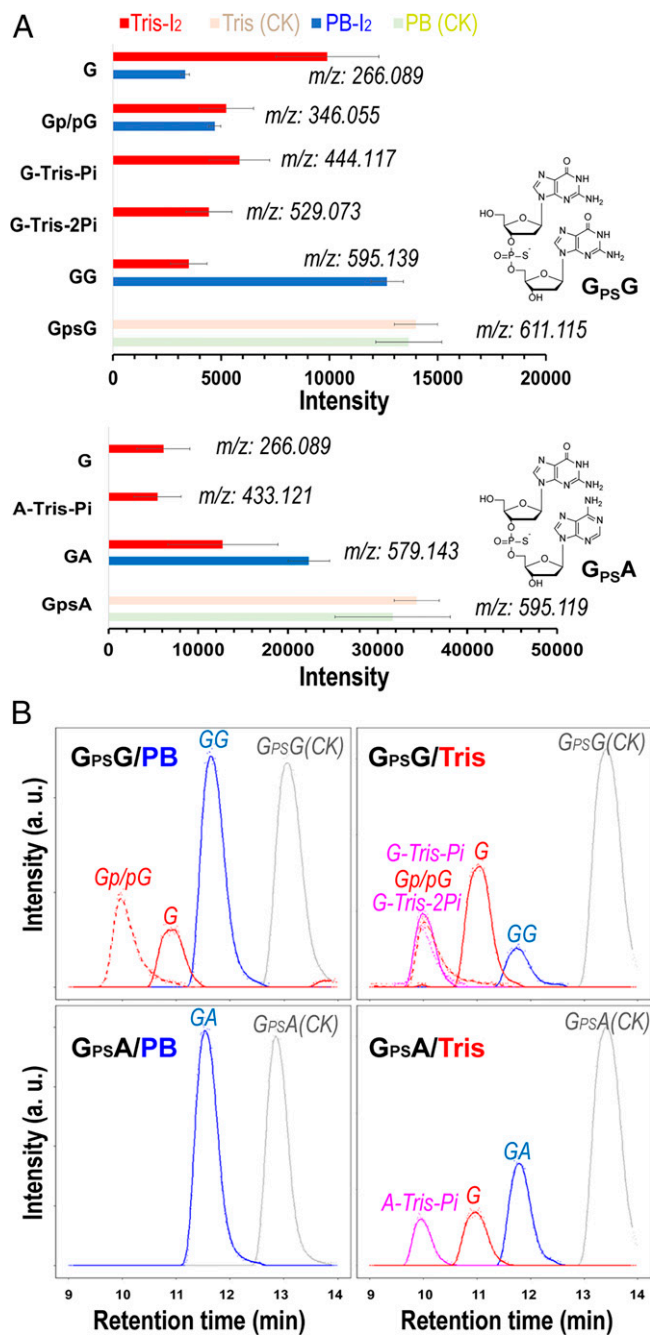
Fig. 8. Iodine-induced cleavage in phosphate buffer (PB) and Tris·HCl buffer (Tris). (A) Comparison of the products and their yields between the $G_{PS}G$ and $G_{PS}A$ PT dinucleotides (intensity in height of MS signals). Red, 2.5 μM PT dinucleotide + 2.0 mM I_2 in 10.0 mM Tris (pH 9.0); blue, 2.5 μM PT dinucleotide + 2.0 mM I_2 in 10.0 mM PB (pH 9.0); light orange, 2.5 μM PT dinucleotide in 10.0 mM Tris (pH 9.0, control); light green, 2.5 μM PT dinucleotide in 10.0 mM PB (pH 9.0, control). No A/pA/A-Tris-2Pi/Gp/G-Tris-Pi/G-Tris-2Pi were observed in the Tris-assisted cleavage of $G_{PS}A$. (B) The extracted ion chromatograms of the iodine-induced products of $G_{PS}G$ and $G_{PS}A$ in PB and Tris (red, the products of P-O cleavage; blue, the products of P-S cleavage; CK, the control samples without adding iodine; the datasets used in B were noted in *SI Appendix*, Figs. S11–S14). a.u., arbitrary unit.

modified sites in *dnd* gene–bioengineering *S. lividans* 1326 and *Escherichia coli* B7A) were used as the PT model compounds for iodine-induced reactions, and the iodine-induced product profiles were measured using high-pressure liquid chromatography-mass spectrometry (HPLC-MS) (8).

As shown in Fig. 8A, using the average mass spectrometry (MS) intensities of non–iodine-phosphorothioate dinucleotide

controls, the P-S/P-O conversion yields reached ~93% and ~62% for $G_{PS}G$ and $G_{PS}A$ in phosphate buffer, respectively, while the yields decreased to ~25% and ~32% in Tris buffer solution (see the raw HPLC-MS data, chromatograms in *SI Appendix*, Figs. S11–S14, and detailed XCMS [various forms (X) of chromatography mass spectrometry] analysis in *SI Appendix*). The dramatic change of P-S/P-O conversion is in good agreement with the calculated results that predict that Tris is involved in the iodine-induced reactions of PT-DNA. The yields of guanine nucleoside, the direct product of bridging P-O cleavage, were ~71% and ~15% for $G_{PS}G$ and $G_{PS}A$ in Tris solution, respectively, and ~24% for $G_{PS}G$ in phosphate buffer, but nondetectable for $G_{PS}A$ in phosphate buffer. A considerable amount of guanine nucleotide (pG or Gp) was observed in the case of $G_{PS}G$ iodine-induced cleavage in both buffers. This result indicates that the P-O cleavage is highly dependent on the chemical environment and DNA sequence (see conformational analysis of $G_{PSI}G$ and $G_{PSI}A$ in *SI Appendix*, Fig. S15).

The evidence for Tris involvement in the P-O cleavage is reflected by the MS signals of G-Tris-Pi ([M-H]⁻, mass-to-charge ratio m/z 449.117)/(+183.028, Tris-phosphate), G-Tris-2Pi ([M-H]⁻, m/z 529.073)/(+262.984, Tris-diphosphate), and A-Tris-Pi([M-H]⁻, m/z 433.121)/(+183.027, Tris-phosphate) (see the plausible structures in *SI Appendix*, Fig. S16). These m/z shifts are in good agreement with the m/z values previously reported in which Tris-phosphate (+183.1) and Tris-diphosphate (+263.1) were measured by the matrix-assisted laser desorption/Ionization time-of-flight (MALDI-TOF) MS (9). In this work, Tris is characterized as a general base for the bridging P-O cleavage, rather than an unwanted contaminant as described in previous studies. More intriguingly, the formation of the Tris-diphosphate derivative implies that one molecule of Tris is involved in two units of phosphorothioate cleavage, which may provide insights into the degree of typical palindromic PT modifications in the PT-DNA genome.

Discussion

Taken together, our results demonstrate that the strong halogen bond between phosphorothioate and iodine conveys an exceptional chemoselectivity for iodine attack at the PT-modified site. The I-I dissociation of the triiodide-like [(PS)-I-I]⁻ XB complex produces the reactive **PSI** species. Although hypoiodous acid can be formed via iodine hydrolysis under the experimental condition, it cannot form a halogen bond with phosphorothioate as strong as iodine does, and its contribution to produce the reactive **PSI** species is negligible (*SI Appendix*, Fig. S17). Moreover, the iodine chemoselectivity for phosphorothioate and phosphate was calculated to be constant at 24.5 kcal/mol after adding polarization and diffuse functions into the iodine LANL2DZ basis set; however, the XB energies decrease by 8.1 and 1.9 kcal/mol, respectively (*SI Appendix*, Tables S1 and S2). In the presence of amines, i.e., DNA bases and Tris, S-N coupling takes place via A_N and produces the **PSN** species. The formation of the S-N bond significantly promotes P-O bond breaking and suppresses the unwanted P-S cleavage. If this were not the case, the hydrolytic P-S cleavage of **PSI** would be overwhelming and no P-O cleavage would be observed. The Tris effect reverses the noncyclic **PSN** preference of P-S and P-O cleavage and leads to the formation of the unstable phosphate triester due to the strain of the PSNCCO six-membered ring in the transient pentacoordinate phosphorane intermediate (see the PSNCCO definition in Fig. 7).

We have discovered that Tris plays critical roles in PT-DNA cleavage. The Tris adducts observed by HPLC-MS appear to be precursors or by-products of terminal hydroxyl DNA fragments, rather than the side products that have been described in previous literature (figure 4 in ref. 9). Our results advocate for the need for more reactive alcohol-amine catalysis. This revelation is based on the observation that both the PT dinucleotide experiment and model calculation indicated that the bridging P-O bond breaking in the iodine-induced PT-DNA cleavage was dependent on neighboring DNA 3′ bases (e.g., guanine C2-NH_2) that might be accessible for the nascent **PSI** species. Otherwise, the **PSI** species could hydrolyze to normal phosphate diester as in Figs. 4 and 8*B* ($G_{PS}A$).

The less efficient P-O bond cleavage implied that the PT-modified site was not fully broken with the iodine treatment and that a considerable fraction of the P-S bonds is transformed to the normal phosphate linkages. This suggests that the bioinformatic analyses need to fully consider the unrealistic assumption of highly efficient cleavage at the PT-modified site, particularly for $G_{PS}A$ sites. On the other hand, the iodine-induced P-S/P-O conversion (direct **PSI** hydrolysis) provides an alternative two-electron antioxidative pathway accompanied by multiple nucleophilic addition and eliminations, which is complementary with the one-electron radical pathways proposed in our previous work on anti-ROS function.

Iodine treatment can cleave bridging P-O bonds at the PT site in the presence of nucleophiles like amines or convert the PT modification to a normal phosphate linkage. These results provide an insightful understanding that helps define PT-DNA cleavage as a XB-guiding and amine-related process, which is consistent with results observed in experiments. Our results also suggest that it is desirable to develop more efficient auxiliary alcohol-amines or diamines to further decrease barriers at the rate-determining step of pentacoordinate phosphorane intermediates for iodine-induced deep sequencing of PT-modified genomes.

Materials and Methods

Experiment. The Tris effect in the iodine-induced PT-DNA cleavage was validated by agarose gel electrophoresis. *E. coli* DH10B cells harboring pJTU1238, which contained the *dnd*B-E functional gene cluster from *Salmonella enterica* and was reported to possess ~1,500 PT modifications per 10^6 nt (35), were used for the validating experiment. The freshly extracted PT-DNA (OD_{260} = 0.5) was treated with 3.0 mM I_2 (10% ethanol solution) in 50 mM (at pH 9.0) phosphate buffer with or without 0.1 mM Tris·HCl, and with or without a 5-min heat shock at 65 °C (9). The reactant mixture was incubated for 15 min. Agarose gel electrophoresis was performed on a 0.8% agarose gel in 1× MOPS electrophoretic buffer (20 mM 3-(*N*-morpholino)propanesulfonic acid [MOPS], 5.0 mM NaAc, and 1.0 mM ethylenediamine tetraacetic acid) at 65 V for 50 min. The gels were stained with GelRed (Biotium) and visualized using the Alphalimager HP gel imaging system.

For experimental validation, both the $G_{PS}G$ and $G_{PS}A$ linkages, which were abundantly available in *dnd*-containing *S. lividans* 1326 and *E. coli* B7A (36), were tested for iodine-induced cleavage. In detail, a mixture of 2.5 μM PT dinucleotide and 2.0 mM I_2 was incubated for 15 min and then analyzed by HPLC-MS on an Agilent HPLC 1290-MS 6230 ultra-performance liquid chromatography (UPLC) time-of-flight mass spectrometry. A 10-μL volume of reaction sample was loaded on Agilent's C18 reversed phase column (150 × 4.6 mm, 3 μm), and water and acetonitrile with 0.1% acetic acid were used as eluent A and eluent B in HPLC, respectively. The flow rate was 0.4 mL/min with a gradient 1% to 13% buffer B for 6 min, 13% to 30% buffer B for another 14 min, and then 30% to 99% buffer B for 2 min. MS was carried out with the 320 °C drying gas flow of 8 L/min, nebulizer pressure of 35 psi, and capillary voltage of 3,500 V. (The detailed materials are described in *SI Appendix*.)

Computation. All stationary point structures were optimized with the empirical dispersion-included ωB97X-D functional (37) in Gaussian 16 (38). The phosphorothioate diester model used in this work is consistent with that used in previous work (39, 40). The prototype and methylamine models were fully optimized with the basis sets of cc-pVTZ (41) for H, N, C, O, P, and S atoms and LanL2DZ for iodine (42). In the hydrolytic steps, transition structures were optimized with the 6-31+G(d) basis set (43) for H, N, C, O, P, and S atoms to allow for less intensive computation in searching the lowest-energy pathways. All lowest-energy conformations were first obtained with the conformer rotamer ensemble sampling tool, using the semiempirical tight binding–based quantum chemistry method GFN2-xTB in the framework of metadynamics (44, 45). All calculations incorporate the SMD implicit solvation model for aqueous solutions (46). Vibrational frequency analyses were performed at the same level of theory to ensure local minima or first-order saddle points, and the free energies were calculated at 298 K. In addition, intrinsic reaction coordinate calculations (47) and relaxed potential surface scans were carried out to identify transition states and immediate reactants and products. In the nucleophilic association-dissociation section, the lowest-energy transition states and intermediates are discussed as representative for each hydrolytic pathway.

The inter- and intramolecular interactions between iodine and phosphorothioate/phosphodiester were interrogated by frontier molecular orbital analysis (48), charge decomposition analysis (49), and independent gradient model analysis (50) in the Multiwfn 3.6 software package (51). The chemical iodine selectivity between the PT-modified site and normal phosphate linkages was simulated by the COPASI 4.27, build 217, package (52), with the above QM-calculated kinetic parameters at the experimental concentration. Isosurface maps were produced using the visual molecular dynamics 1.9.3 program (53) based on outputs from the Multiwfn calculations. Houk model representation was used in the CYLview visualization of the calculated structures (54).

Author affiliations: [a]State Key Laboratory of Microbial Metabolism, School of Life Sciences and Biotechnology, Shanghai Jiao Tong University, Shanghai 200240, China; [b]Joint International Research Laboratory of Metabolic and Developmental Sciences, School of Life Sciences and Biotechnology, Shanghai Jiao Tong University, Shanghai 200240, China; and [c]Department of Chemistry and Biochemistry, University of California, Los Angeles, CA 90095

1. J. Liang *et al.*, DNA modification by sulfur: Analysis of the sequence recognition specificity surrounding the modification sites. *Nucleic Acids Res.* **35**, 2944–2954 (2007).
2. X. Xiong *et al.*, SspABCD-SspE is a phosphorothioation-sensing bacterial defence system with broad anti-phage activities. *Nat. Microbiol.* **5**, 917–928 (2020).
3. T. Tong *et al.*, Occurrence, evolution, and functions of DNA phosphorothioate epigenetics in bacteria. *Proc. Natl. Acad. Sci. U.S.A.* **115**, E2988–E2996 (2018).
4. G. Liu *et al.*, Structural basis for the recognition of sulfur in phosphorothioated DNA. *Nat. Commun.* **9**, 4689 (2018).
5. H. Yu *et al.*, DNA backbone interactions impact the sequence specificity of DNA sulfur-binding domains: Revelations from structural analyses. *Nucleic Acids Res.* **48**, 8755–8766 (2020).
6. X. Xie *et al.*, Phosphorothioate DNA as an antioxidant in bacteria. *Nucleic Acids Res.* **40**, 9115–9124 (2012).
7. T. Wu *et al.*, Mechanistic investigation on ROS Resistance of phosphorothioated DNA. *Sci. Rep.* **7**, 42823 (2017).
8. Q. Huang *et al.*, Defense mechanism of phosphorothioated DNA under peroxynitrite-mediated oxidative stress. *ACS Chem. Biol.* **15**, 2558–2567 (2020).

9. B. Cao et al., Genomic mapping of phosphorothioates reveals partial modification of short consensus sequences. *Nat. Commun.* **5**, 3951–3963 (2014).

10. J. Li et al., Quantitative mapping of DNA phosphorothioate reveals phosphorothioate heterogeneity of low modification frequency. *PLoS Genet.* **15**, e1008026 (2019).

11. Y. Chen et al., Novel iodine-induced cleavage real-time PCR assay for accurate quantification of phosphorothioate modified sites in bacterial DNA. *Sci. Rep.* **9**, 7485 (2019).

12. S. Kellner, Oxidation of phosphorothioate DNA modifications leads to lethal genomic instability. *Nat. Chem. Biol.* **13**, 888–894 (2017).

13. Z. Hu et al., Site-specific scissors based on myeloperoxidase for phosphorothioate DNA. *J. Am. Chem. Soc.* **143**, 12361–12368 (2021).

14. K. L. Nakamaye, G. Gish, F. Eckstein, H.-P. Vosberg, Direct sequencing of polymerase chain reaction amplified DNA fragments through the incorporation of deoxynucleoside alpha-thiotriphosphates. *Nucleic Acids Res.* **16**, 9947–9959 (1988).

15. G. Gish, F. Eckstein, DNA and RNA sequence determination based on phosphorothioate chemistry. *Science* **240**, 1520–1522 (1988).

16. F. H. Westheimer, Why nature chose phosphates. *Science* **235**, 1173–1178 (1987).

17. S. C. L. Kamerlin, P. K. Sharma, R. B. Prasad, A. Warshel, Why nature really chose phosphate. *Q. Rev. Biophys.* **46**, 1–132 (2013).

18. G. K. Schroeder, C. Lad, P. Wyman, N. H. Williams, R. Wolfenden, The time required for water attack at the phosphorus atom of simple phosphodiesters and of DNA. *Proc. Natl. Acad. Sci. U.S.A.* **103**, 4052–4055 (2006).

19. Y. Liu, B. A. Gregersen, A. Hengge, D. M. York, Transesterification thio effects of phosphate diesters: Free energy barriers and kinetic and equilibrium isotope effects from density-functional theory. *Biochemistry* **45**, 10043–10053 (2006).

20. B. A. Gregersen, X. Lopez, D. M. York, Hybrid QM/MM study of thio effects in transphosphorylation reactions. *J. Am. Chem. Soc.* **125**, 7178–7179 (2003).

21. P. Metrangolo, H. Neukirch, T. Pilati, G. Resnati, Halogen bonding based recognition processes: A world parallel to hydrogen bonding. *Acc. Chem. Res.* **38**, 386–395 (2005).

22. A.-C. C. Carlsson et al., Solvent effects on halogen bond symmetry. *CrystEngComm* **15**, 3087–3092 (2013).

23. J. Purcell, A. C. Hengge, The thermodynamics of phosphate versus phosphorothioate ester hydrolysis. *J. Org. Chem.* **70**, 8437–8442 (2005).

24. P. R. Young, P. E. McMahon, Iodide reduction of sulfilimines. Evidence for the partitioning of sulfurane intermediates. *J. Am. Chem. Soc.* **107**, 7572–7577 (1985).

25. W. A. Henderson Jr., C. J. Schultz, The nucleophilicity of amines. *J. Org. Chem.* **27**, 4643–4646 (1962).

26. J. Florián, A. Warshel, Phosphate ester hydrolysis in aqueous solution: Associative versus dissociative mechanisms. *J. Phys. Chem. B* **102**, 719–734 (1998).

27. A. J. Kirby, F. Nome, Fundamentals of phosphate transfer. *Acc. Chem. Res.* **48**, 1806–1814 (2015).

28. F. Duarte, J. Åqvist, N. H. Williams, S. C. L. Kamerlin, Resolving apparent conflicts between theoretical and experimental models of phosphate monoester hydrolysis. *J. Am. Chem. Soc.* **137**, 1081–1093 (2015).

29. D. Petrović, K. Szeler, S. C. L. Kamerlin, Challenges and advances in the computational modeling of biological phosphate hydrolysis. *Chem. Commun. (Camb.)* **54**, 3077–3089 (2018).

30. J. Florián, A. Warshel, A fundamental assumption about OH⁻ attack in phosphate ester hydrolysis is not fully justified. *J. Am. Chem. Soc.* **119**, 5473–5474 (1997).

31. R. F. Bayfield, E. R. Cole, Sulfenamides and sulfinamides conjugative affinity and pKa values of aryl sulfonamides. *Phosphorus Sulfur Silicon Relat. Elem.* **45**, 237–242 (1989).

32. R. J. Gillis, P. Lolur, W. H. Green, H_2 generation from H_2O and H_2S through an iodine cycle. *ACS Sustain. Chem. Eng.* **7**, 7369–7377 (2019).

33. L. Craine, M. Raban, The chemistry of sulfenamides. *Chem. Rev.* **89**, 689–712 (1989).

34. R. A. Lazarus, S. J. Benkovic, Mechanism of hydrolysis of phosphorylethanolamine triesters. Multiple catalytic effects of an intramolecular amino group. *J. Am. Chem. Soc.* **101**, 4300–4312 (1979).

35. L. Wang et al., Phosphorothioation of DNA in bacteria by *dnd* genes. *Nat. Chem. Biol.* **3**, 709–710 (2007).

36. L. Wang et al., DNA phosphorothioation is widespread and quantized in bacterial genomes. *Proc. Natl. Acad. Sci. U.S.A.* **108**, 2963–2968 (2011).

37. J. D. Chai, M. Head-Gordon, Long-range corrected hybrid density functionals with damped atom-atom dispersion corrections. *Phys. Chem. Chem. Phys.* **10**, 6615–6620 (2008).

38. M. J. Frisch et al., *Gaussian 16 Software, Revision A.03* (Gaussian, Inc., Wallingford, CT, 2016).

39. Y.-C. Zhang et al., Theoretical study on steric effects of DNA phosphorothioation: B-helical destabilization in Rp-phosphorothioated DNA. *J. Phys. Chem. B* **116**, 10639–10648 (2012).

40. L. Chen et al., Theoretical study on the relationship between Rp-phosphorothioation and base-step in S-DNA: Based on energetic and structural analysis. *J. Phys. Chem. B* **119**, 474–481 (2015).

41. T. H. Dunning Jr., Gaussian basis sets for use in correlated molecular calculations. I. The atoms boron through neon and hydrogen. *J. Chem. Phys.* **90**, 1007–1023 (1998).

42. W. R. Wadt, P. J. Hay, Ab initio effective core potentials for molecular calculations – Potentials for main group elements Na to Bi. *J. Chem. Phys.* **82**, 284–298 (1985).

43. V. A. Rassolov, M. A. Ratner, J. A. Pople, P. C. Redfern, L. A. Curtiss, 6-31G* basis set for third-row atoms. *J. Comput. Chem.* **22**, 976–984 (2001).

44. P. Pracht, F. Bohle, S. Grimme, Automated exploration of the low-energy chemical space with fast quantum chemical methods. *Phys. Chem. Chem. Phys.* **22**, 7169–7192 (2020).

45. S. Grimme, Exploration of chemical compound, conformer, and reaction space with meta-dynamics simulations based on tight-binding quantum chemical calculations. *J. Chem. Theory Comput.* **15**, 2847–2862 (2019).

46. A. V. Marenich, C. J. Cramer, D. G. Truhlar, Universal solvation model based on solute electron density and on a continuum model of the solvent defined by the bulk dielectric constant and atomic surface tensions. *J. Phys. Chem. B* **113**, 6378–6396 (2009).

47. S. Maeda, Y. Harabuchi, Y. Ono, T. Taketsugu, K. Morokuma, Intrinsic reaction coordinate: Calculation, bifurcation, and automated search. *Int. J. Quantum Chem.* **115**, 258–269 (2015).

48. V. Angarov, S. Kozuch, On the σ, π and δ hole interactions: A molecular orbital overview. *New J. Chem.* **42**, 1413–1422 (2018).

49. F. R. Wagner, V. Bezugly, M. Kohout, Y. Grin, Charge decomposition analysis of the electron localizability indicator: A bridge between the orbital and direct space representation of the chemical bond. *Chemistry* **13**, 5724–5741 (2007).

50. C. Lefebvre et al., Accurately extracting the signature of intermolecular interactions present in the NCI plot of the reduced density gradient versus electron density. *Phys. Chem. Chem. Phys.* **19**, 17928–17936 (2017).

51. T. Lu, F. Chen, Multiwfn: A multifunctional wavefunction analyzer. *J. Comput. Chem.* **33**, 580–592 (2012).

52. S. Hoops et al., COPASI–A COmplex PAthway SImulator. *Bioinformatics* **22**, 3067–3074 (2006).

53. W. Humphrey, A. Dalke, K. Schulten, VMD: Visual molecular dynamics. *J. Mol. Graph.* **14**, 33–38, 27–28 (1996).

54. C. Y. Legault, *CYLview20* (Universite de Sherbrooke, Quebec, Canada, 2020). https://www.cylview.org/.